Tavakoli, Sasan; Shaghaghi, Poorya; Mancini, Simone; De Luca, Fabio; Dashtimanesh, Abbas

Wake waves of a planing boat : An experimental model

Published in:
PHYSICS OF FLUIDS

DOI:
10.1063/5.0084074

Published: 01/03/2022

Document Version
Publisher's PDF, also known as Version of record

Published under the following license:
Unspecified

Please cite the original version:
Tavakoli, S., Shaghaghi, P., Mancini, S., De Luca, F., & Dashtimanesh, A. (2022). Wake waves of a planing boat : An experimental model. *PHYSICS OF FLUIDS*, *34*(3), [037104]. https://doi.org/10.1063/5.0084074

Physics of Fluids

Wake waves of a planing boat: An experimental model

Cite as: Phys. Fluids **34**, 037104 (2022); https://doi.org/10.1063/5.0084074
Submitted: 03 January 2022 • Accepted: 04 February 2022 • Published Online: 03 March 2022

Sasan Tavakoli, Poorya Shaghaghi, Simone Mancini, et al.

Physics of Fluids ARTICLE scitation.org/journal/phf

Wake waves of a planing boat: An experimental model

Cite as: Phys. Fluids **34**, 037104 (2022); doi: 10.1063/5.0084074
Submitted: 3 January 2022 · Accepted: 4 February 2022 ·
Published Online: 3 March 2022

Sasan Tavakoli,[1,2,a)] Poorya Shaghaghi,[3,b)] Simone Mancini,[4,c)] Fabio De Luca,[5,d)] and Abbas Dashtimanesh[6,7,e)]

AFFILIATIONS

[1]Department of Infrastructure Engineering, The University of Melbourne, Victoria 3052, Australia
[2]Department of Mechanical Engineering, Aalto University, 02150 Espoo, Finland
[3]Department of Mechanical Engineering, The University of Melbourne, Victoria 3052, Australia
[4]Department of Hydro and Aerodynamics, Force Technology, Kgs. Lyngby 2800, Denmark
[5]Department of Industrial Engineering, University of Naples "Federico II," Naples 80125, Italy
[6]Estonian Maritime Academy, Tallinn University of Technology, Kopli, 11712 Tallinn, Estonia
[7]Center for Naval Architecture, School of Engineering Science, KTH Royal Institute of Technology: Kungliga Tekniska Hogskolan, Brinellvägen 8, 114 28 Stockholm, Sweden

[a)]**Author to whom correspondence should be addressed:** stavakoli@student.unimelb.edu.au
[b)]**E-mail**: pshaghaghi@student.unimelb.edu.au
[c)]**E-mail**: simo@force.dk
[d)]**E-mail**: fabio.deluca@unina.it
[e)]**E-mail**: abbasda@kth.se

ABSTRACT

The wake waves generated by the steady movement of a planing hull are analyzed by means of towing tank tests. Two sets of waves, including divergent and transverse waves, are identified and then analyzed. The wave period of the divergent waves is seen to decrease by the increase in speed of the vessel. These waves are seen to damp temporally. The mechanisms that lead to damping of the divergent wave were found to depend on the wave orbital Reynolds number in semi-planing regime, though that of in-planing regime is a function of the Reynolds number of the boat. The wake angle is seen to decrease with the increase in Froude number, the rate of which becomes relatively large in-planing regime. Transverse waves are captured through measurements, and it is shown that while their period is longer than those of the divergent waves, they are not noticeably damped. Throughout the spectral analysis, it is demonstrated that divergent waves reach a higher level of nonlinearity by the increase in Froude number and, hence, the wave energy is distributed over a boarder range of frequency. The height of the transverse wave is observed to become lower by the increase in speed, but as the towing speed increases, the probability density function curves of surface elevation deviate more and more from the Gaussian distribution.

I. INTRODUCTION

Any solid body moving on the interface between water and air causes a disturbance in the free surface, which is known as wake (Lamb, 1932 and Darrigol, 2005). The underlying mechanism that leads to the generation of the wake is the pressure variation at the air–sea interface (Wu *et al.*, 2019 and Colen and Kolomeisky, 2021), which is excited by the steady movement of the solid body. Wake has a V-shaped pattern, which was first discovered by Kelvin in 1887 (Thomson and Kelvin, 1887). Two sets of waves including divergent and transverse waves are generated by the forward steady motion of the solid body. The energy of these two sets of waves is confined in a wedge with a half-angle of $\sin^{-1}(1/3) = 19.47°$, which is known as the Kelvin angle (Havelock, 1908; Ursell *et al.*, 1960; Sorensen, 1973; and Yih and Zhu, 1989). While the wake of ships is a beautiful physical phenomenon that can frequently be observed in nature (Yuan *et al.*, 2021), the wake-induced waves have become a major worry in the past two decades. The wake-driven waves caused by high-speed ships and boats travel at a fast speed, and their energy may not necessarily be damped in the sea. The heavy traffic of fast ships has been recognized as a potentially damaging mechanism in waterways, wetlands, and shallow water environments (Parnell and Kofoed-Hansen, 2001; Bauer *et al.*, 2002; and Bilkovic *et al.*, 2017). Boat wake policies and

regulatory frameworks have been enacted to protect the potential damaging regions (Bilkovic *et al.*, 2019). To adopt these rules properly, the physics of the problem needs to be understood well.

As mentioned, the wake waves of high-speed ships propagate at a fast speed and can be highly energetic (Keller, 1970; Stumbo *et al.*, 1999; Whittaker and Elsässer, 2002; Benassai *et al.*, 2013; Darmon, 2014; and He *et al.*, 2020), one that might be viewed as a model of rogue waves in the coastal environment (Wu, 1987; Pedersen, 1988; and Torsvik *et al.*, 2015). Our understanding of the physics of the wake waves of high-speed ships/ferries has been formed through field measurements in the past decade (Wyatt and Hall, 1988; Begovic *et al.*, 2007; and Benassai *et al.*, 2015). Also, radar images have been processed to analyze the wake of high-speed boats most recently (Reed and Milgram, 2002). Wake waves of high-speed ships are nonlinear and the wake wedge (i.e., lateral extent of the wake waves) of vessels advancing at high speed is found to get narrower by the increase in the speed of the vessel (Nobless *et al.*, 2014). The turbulent flow behind the vessel might lead to the decay of the energy level of wake waves (Patel and Sarda, 1990).

Among various types of fast boats/ships used for maritime transportation, planing hulls have been known as the most popular ones (Savitsky, 1964 and Savitsky, 1985). These hulls can reach relatively high speed by skimming on the water surface (Naghdi and Rubin, 1981). The bottom surface of planing surfaces acts similarly to a lifting surface on which hydrodynamic and hydrostatic forces together support the weight (Cumberbatch, 1958 and McCauley, 2018). The bow of the vessel is pitched up by the water flow, which in turn minimizes the bow wave-making drag force (Chung and Chun, 2007). This mechanism provides the opportunity for the vessel to positions its center of gravity at a higher level compared to the initial position. When a vessel rides in such a condition, waves generated near the bow of the vessel become short and small amplitude as the submergence of the vessel and its wetted length are both scant. This enables the vessel to reach relatively high speeds as both waves generated near the bow of the vessel and the wetted surface of the vessel are small.

The stern of planing hulls is commonly designed to have a transom shape, which is beneficial at high-speeds. When the vessel reaches high speeds, the transom gets dry, and consequently, water separation from the transom occurs (Tuck *et al.*, 2002). This causes strong turbulent flow in the lee of the vessel. Water moves downward just behind the vessel, and then, it rises, reaching a high level. The generated water surface profile behind the vessel is known as the transom wave or the rooster tail (Savitsky, 1988 and Doctors, 2003). The rooster tail profile has been well documented by van Dyck in 1960 (van Dyck, 1960). The area located in between the rooster tail and the dry transom is identified as the hollow region, which is formed due to the flow separation from the transom [Fig. 4.18 of Faltinsen (2005) describes the generation of the free surface behind the vessel]. If the transom stern does not get fully dried, the depth of the hollow might be lower.

The rooster tail moves forward with the vessel. Large pressure variation emerging near the rooster tail causes the wake waves. This makes the wake waves generated by planing hulls different from that of high-speed ships. The presence of the transom waves can cause the mixing of turbulent layers and make the wake waves strongly turbulent (O'Dea *et al.*, 1981 and Lyden *et al.*, 1988). The turbulent fluid motion in the lee of the vessel is expected to affect the generation of waves (Peregrine, 1971).

The importance of the fluid field behind the planing hulls and the high-speed vessel has been highlighted during the last three decades [see, e.g., Faltinsen and Zhao (1991); Garland and Maki (2012); and Mousaviraad *et al.* (2015)]. Researchers attempted to identify the shape of the water surface elevation just behind the vessel. For instance, Savitsky and Morabito (2010) performed systematic studies to measure the water surface profile just behind a planing hull. Maki *et al.* (2006, 2008) also performed similar measurements, but over the range of lower Froude numbers by attempting to find the link between the near transom pressure and the wave steepness just behind it. Both of these studies have been performed to understand the water surface elevation just behind the transom stern of the vessel. The main reason was that authors were interested to know when the transom gets dry and how the transom wake pattern can be utilized to model the stepped planing hulls (Niazmand Bilandi *et al.*, 2021). It is worth noting that steps are believed to act similarly to a transom stern causing air ventilation on a large area of the vessel, which can significantly contribute to improved performance of a vessel. Thus, researchers were highly motivated to find the flow surface pattern behind the transom to be employed in performance prediction models.

While the need to understand the near transom wake has pushed researchers to perform experimental studies to measure the transom waves, the wake pattern of planing hulls and the wake waves of these hulls have not received as much attention as they deserve. Limited research has been performed highlighting the wake pattern. Most of the previous research have focused on the case of disk advancing in planing regime or by using the Google images (Moisy and Rabaud, 2014a and Darmon *et al.*, 2014). When waves are generated by a moving disk, no flow separation from the transom occurs. Experimental measurements highlighting the wake of a planing hull are needed to be performed in the first place. This helps us to go beyond the limitations by understanding (I) the shape of the wakes behind a vessel advancing in the planing regime and (II) the water wave motion caused by the vessel. Such a study might be carried out by field measurements. However, with field measurements, it is difficult to single out the effect of one physical phenomena, as other governing physics such as swell and wind occur simultaneously (note that wind can affect the water due to the possible air–water momentum exchange, see, e.g., Eeltink *et al.*, 2017; Zavadsky and Shemer, 2017; Zavadsky *et al.*, 2017; and Jou and Lo, 2020). To this end, it is vital to perform systematic controlled laboratory studies in towing tanks [see, e.g., Caplier *et al.* (2016) and Wang and Chen (2017)].

Computational methods can be also used to reconstruct the wake waves generated by planing hulls through solving the viscous air–water flow in a numerical tank. There are several computational studies in the literature providing detailed analyses on the wake behind a planing hull (Gray-Stephens *et al.*, 2020; De Luca *et al.*, 2016; Ghadimi *et al.*, 2015; Suneela *et al.*, 2020; and Tagliafierro *et al.*, 2021). Using steady simulation setups, authors have reproduced the water surface elevation pattern in the near wake field of the boat with an acceptable level of accuracy, though they did not highlight the temporal development of water waves. The lack of experimental studies and the need to consider a large computational domain are perhaps the main reasons that authors did not pay attention to the time history of ship-generated waves in their computational studies. Therefore, it is necessary to

TABLE I. Main particulars of towing tank of the "University of Naples."

Parameter	Value	Unit
Length of the tank	137.0	m
Width of the tank	9.0	m
Depth of the tank	4.25	m
Maximum carriage speed	10.0	m/s

perform an early study on the wake waves of planing hulls through towing tank tests.

The present paper aims to fill the gaps in the knowledge of wake waves of a hard-chine planing hull by using the towing tank tests. Tests are performed for four different speeds covering both semi and full planing regimes. Water surface elevation is recorded by four different probes. Temporal evolution of waves, including divergent and transverse, together with the wake angle are analyzed. The rest of the paper is structured as follows. Section II presents the experimental setup used to study the problem. Section III outlines the test plans of the research. Sections III A and III B present the divergent and transverse wave results. Concluding remarks are presented in Sec. IV. The calm-water performance of the vessel is reported in the Appendix.

II. EXPERIMENTAL MODEL

Experiments are conducted in the towing tank of the University of Naples "Federico II" in 2018. The tank is 137 m long, 9 m wide, and with a water depth of 4.25 m. An artificial beach is located at the end of the tank and two floating dampers on the side to damp the waves. That is, in the case, water waves propagate in the basin, and their energy is not reflected. This tank has been used for different experimental tests, most of which highlight the dynamic of ships and high-speed vessels in calm and rough water conditions. All the tests are performed at a temperature of ∼21 °C (room temperature). Details of the tank are outlined in Table I. The front view of the tank carriage can be seen in Fig. 1.

A 2.6-m-long planing vessel, made up of wood, is constructed in the workshop of the towing tank of the University of Naples Federico II. The maximum length of the boat, also known as the length of overall (L_{OA}), is 2.61 m. The boat length at the waterline (L_{WL}) is 2.31 m. This vessel is a warped hull with a beam of 0.74 m (the width of the boat at the waterline, which also equals the distance between two chines). Identified as the maximum width of the boat, the beam of overall (B_{OA}) is 0.865 m.

The vessel is the parent hull of a systematic series of warped planing hulls called NSS (New Systematic Series), De Luca and Pensa, 2017. The deadrise angle (β), the angle between the body line and the calm water in transverse view, is 13° at the transom section, while the deadrise angle of the amidship section is nearly 22.5°. The vessel weighs 106.07 kg, which is normalized by using $\rho g B^3$. The non-dimensional weight of the vessel is 0.225, which can be considered as a relatively light range for high-speed vehicles [readers who are interested to know more about the classification of high-speed planing boats based on their weight force are referred to Fridsma (1969) along with Judge and Judge (2013)]. The boat draft, shown with d, is 0.164 m in a zero towing speed condition. Note that the boat draft refers to vertical distance from the baseline to waterline (see Fig. 2). Principal characteristics of the boat are shown in Table II.

FIG. 1. A front view of the carriage of the University of Naples Federico II towing tank.

As can be seen in Fig. 2, the vessel has a hard-chine body form. The presence of chines leads to the emergence of the Kutta condition at the side edges of the vessel. The body has a transom stern, which gets dried in the high-speed performance. This might benefit the vessel by reducing the drag force acting on the body.

A carriage is used to tow the vessel forward at desired towing speed. The motions of the vessel in transverse and horizontal planes are restrained. The vessel has only two degree of freedom (DoF)—the heave and pitch motions. Thus, the boat has no yaw and roll motions. This ensures that the boat is towed in asymmetric condition. Assuming that the advancement of the boat does not lead to an asymmetric fluid motion pattern, symmetry of experiments was not tested. It is worth noting that an asymmetric motion, which may occur for yawed and heeled conditions (Niazmand Bilandi *et al.*, 2020), can lead to an asymmetric flow pattern, influencing the proprieties of ship-generated water waves (Moisy and Rabaud, 2014b and Pethiyagoda, 2021).

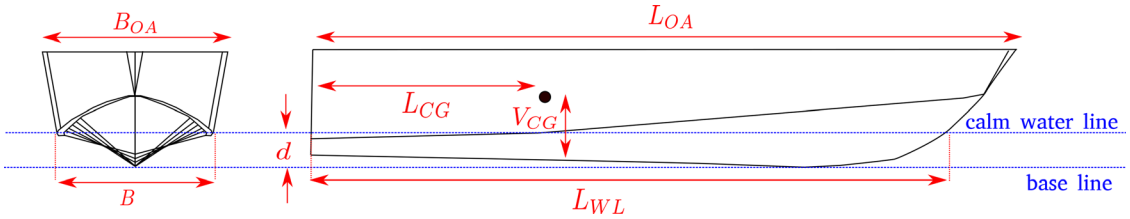

FIG. 2. Body lines (left) and longitudinal view (right) of the planing model tested in the present research.

TABLE II. Main particulars of the planing hull model.

Parameter	Value	Unit
L_{OA}	2.611	(m)
L_{WL}	2.387	(m)
B_{OA}	0.865	(m)
B	0.737	(m)
d at zero towing speed condition	0.164	(m)
L_{WL}/B	3.23	$(\cdots)$
L_{CG}/L_{WL}	0.394	$(\cdots)$
V_{CG}/B	0.501	$(\cdots)$
Δ	106.07	(kg)
β at transom	13.2	deg
β at amidship	22.3	deg

The vessel is towed forward with a constant speed over ∼100 m. Dynamic equilibrium between fluid forces, including hydrostatic force and hydrodynamic lift, occurs in the vertical plane. In addition, the pitching moment acting on the vessel converges zero; that is, the center of pressure is positioned on the pivot point. Thus, the vessel operates in a steady condition, which is identified as the steady planing motion.

The drag force acting on the vessel is caused by the viscous resistance components (flat plate friction, form effect on friction, and viscous pressure) and wave resistance components (wave pattern and wave breaking resistances). All these force components are identified as the resistance force of the vessel.

As the vessel balances, the forces in a vertical direction and the center of pressure are positioned on the pivot point, and the bow is pitched up and the vessel is lifted. This means that the vessel is running at a constant pitch angle, and the pivot point has reached a higher level compared to its initial value. The constant pitch angle is identified as the dynamic trim angle. The height of the pivot point, with respect to the calm water line, is identified as the center of gravity (CG) rise-up. The set of data, presenting the velocity-dependent values of dynamic trim angle, CG rise-up, and resistance forces are known as the calm water performance results, which are used for the design of the vessel. A schematic of the test plan is presented in Fig. 3. The dynamic trim angle and the CG rise-up values of the boat are presented in the Appendix.

Wave probes are located on the water surface to record the propagation of the waves generated by the motion of the vessel, and they are composed of arcs that cross the free surface. An array of probes is located in the middle of the tank, placed some distance away from the hull.

These probes are capacitive gauges with the data logger which samples the water surface elevation at a frequency of 500 Hz, to overcome aliasing. The probes are all positioned on the left side of the vessel, as the water waves generated by the planing motion are expected to be symmetric with respect to the longitudinal plane passing through the centerline of the vessel (see Fig. 3). These are synchronized with the passage of the carriage through a proximity probe; in this way, it is

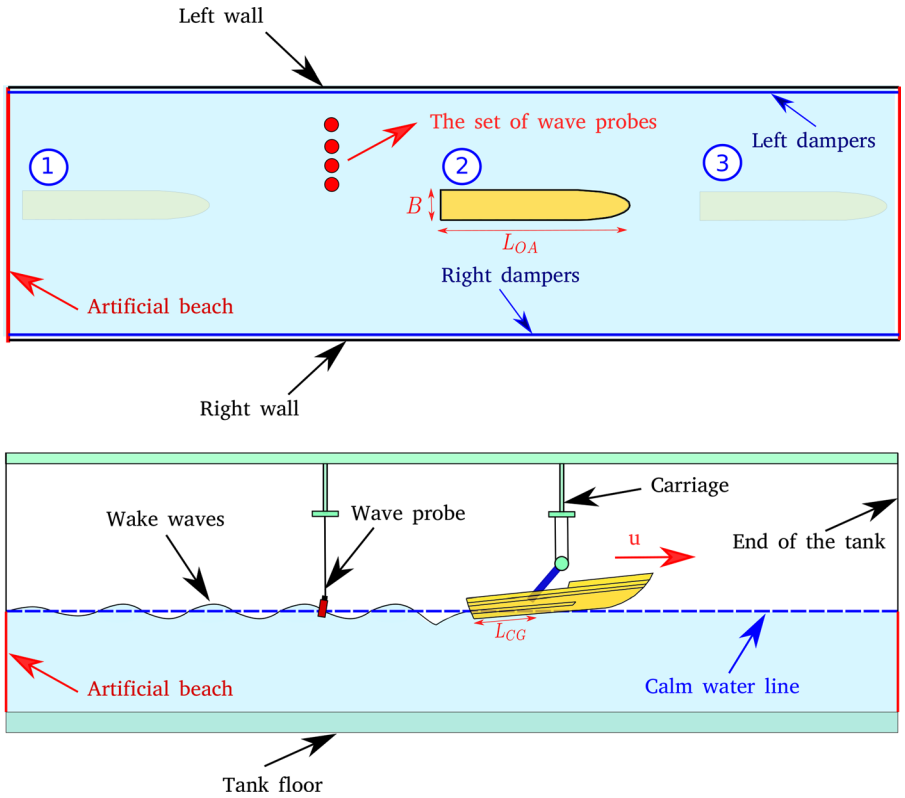

FIG. 3. Schematic of the tests performed to measure the wake waves of a planing hull. Up and lower panels, respectively, show the top and longitudinal views. The vessel is initially at rest (1). Then, it is towed and waves are generated by the hull (2). Eventually, the vessel stops (3). The generated waves are damped by the artificial beach placed at the beginning of the tank and trough the side dumpers. Four wave probes are used to record the water surface elevation.

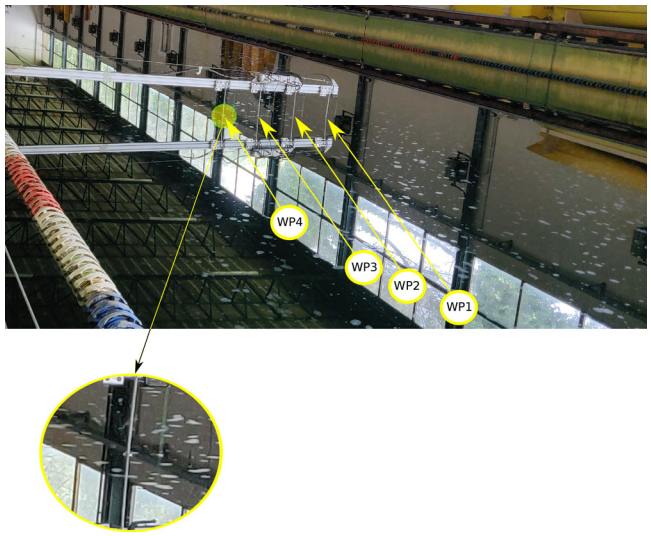

FIG. 4. The four wave probes used to record the water surface elevation, generated by the motion of the boat. A close-up view of the WP4 is shown in a circle below the picture. Note that the reflection of the wave probes by the water surface may be seen in the pictures. Each arrow points to one of the probes.

possible to determine the position of the model relative to the data acquired by the sensors fixed to the side of the tank. Note that, as mentioned earlier, no motion in transverse and horizontal planes is allowed which ensures that the wake pattern is symmetric to the centerline. These probes are, respectively, 1.62B (WP1), 2.02B (WP2), 2.42B (WP3), and 2.82B (WP4) far from the centerline of the vessel. The probes installed in the wave tank can be seen in Fig. 4.

III. TESTS

Tests are performed at four different towing speeds, including 4.0, 5.0, 6.0, and 7.0 m/s. The towing speed is normalized by $\sqrt{gB}$, where g is the gravity acceleration constant and B is the beam of the vessel. The normalized towing speed represents the beam Froude number, which is denoted with Fr_B. The values of towing speeds correspond to beam Froude numbers of 1.5, 1.8, 2.2, and 2.6, which covers semi-planing ($1.0 < Fr_B < 2.0$) and planing regime $Fr_B > 2.0$ [see Savitsky and Brown (1976)]. This helps us gain a better understanding of the physic of the problem. The Reynolds number of the boat ranges between 1.08×10^7 (corresponding to towing speed of 4.0 m/s) and 1.89×10^7 (corresponding to towing speed of 7.0 m/s). Note that the definition of the Reynolds number is presented in Sec. IV. Some photos taken during each test are shown in Fig. 5. As can be seen in Fig. 5, the bow of the vessel is pitched up, and the boat is placed at a high vertical level in all panels. This confirms that the vessel is advancing in the semi-planing and full planing mode.

The water surface is seen to be affected by the advanced movement of the boat. Near the bow of the vessel, where the water jet reaches chine, water spray occurs. The fluid particles are expected to follow a projectile motion pattern over there. The energy of water spray is expected to be dissipated just after moving apart from the vessel. A slight elevation in the water surface might occur near the bow of the vessel. As the vessel bow submergence is negligible, the related water surface elevation is not noticeable. It is interesting to note that the planing motion of the vessel, which leads to the skimming of the vessel on the water surface, is the main reason for the minimization of the wave-making resistance.

Apart from the water spray, occurring near the bow of the vessel, flow is separated from the transom of the vessel. Clear support is observed in all panels of Fig. 5. Water leaves the transom at a relatively high speed. This leads to the development of a hollow, spanning over the beam of the vessel, just behind the stern of the vessel. Water surface, then, reaches a peak value, and the waves, including the transverse and the divergent, are generated. As the typical behavior of the planing hull, the increase in towing speeds leads to the reduction of dynamic trim and sinkage and this is the main reason for the reduction of the hollow and the related crest generated by the hull.

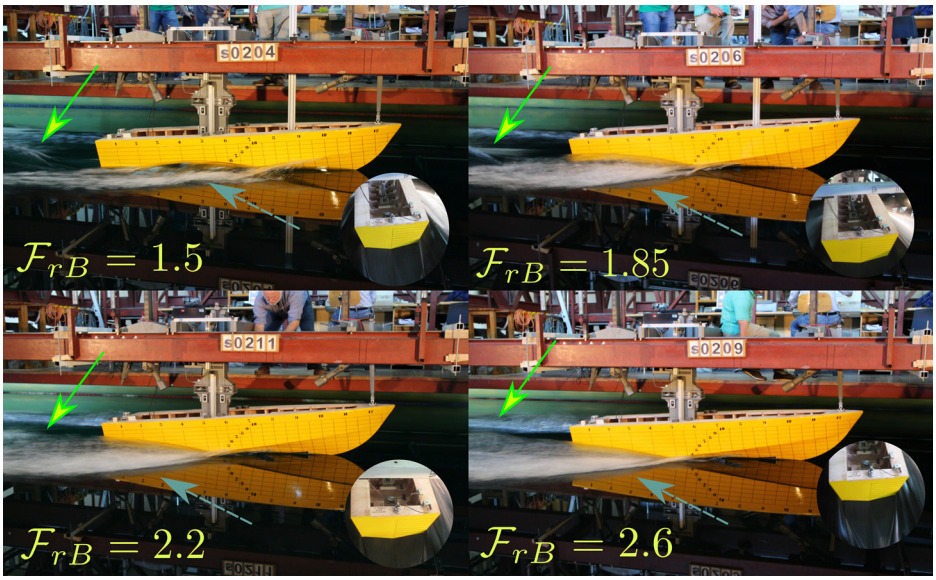

FIG. 5. Photos were taken during the advancement of the vessel. Photos presented in each panel correspond to a specific Froude number. Photos demonstrating that the transom is fully dry during the tests are also shown in the corner of each panel. Green arrows point to the rooster tail, emerged behind the vessel. Dashed arrows point to the water spray generated around the vessel. The water spray height is relatively large for the case of the two highest towing speeds.

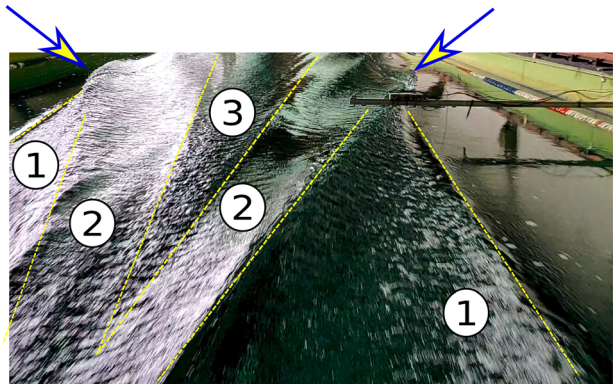

FIG. 6. Water surface elevation behind the vessel. Water surface elevation caused by the pressure variation near the stagnation line of the vessel can be seen in Region 1. Divergent waves occur in Region 2. Transverse waves can be seen in Region 3.

Figure 6 shows the waves generated behind the vessel. The yellow arrows are pointing to the divergent wave in this figure.

A picture showing the water surface profile behind the vessel is shown in Fig. 6. The probes record the water surface elevation caused by the planing motion of the vessel. First, they capture the water surface elevation related to the waves generated near the stagnation line. The region labeled with number 1 shows the related water surface elevation. The pressure is relatively large around there and thus pushes the water down. The kinematic energy of the water jet moving on the wall of the vessel is responsible for this wave [see more details in Payne (1994)]. Then, every single probe records the water surface elevation corresponding to the divergent wave. The region labeled with number 2 shows the related waves. The divergent waves are large, and they are damped as they travel toward the left and right walls of the tank. Two arrows show the damping process of the divergent wave. Finally, probes sample transverse waves, which can be seen in the region labeled with the number 3. Results are presented in Sec. IV of the paper.

A. An overview of the results

Examples of the time histories of the water surfaces recorded by the wave probes are presented. These plots inform the order of the sampling of waves by the wave proves. In addition, the time history of the recorded wave provides an understanding of the temporal evaluation of the water waves at any probe. This can help us analyze the data in Secs. III B and III C.

Figure 7 shows the time history of the recorded waves at four different plots. The results correspond to two different towing speeds of 4.0 and 7.0 m/s. As expected, waves reach the first probe located at $y = 1.62B$ earlier. This probe is the closest to the vessel, and it records the waves earlier. As seen, a trough has emerged first. This trough is related to the concave shape, caused by the hollow behind the vessel. The trough is deeper at the first probe and gets closer to the equilibrium line, $\eta = 0$, as the distance of the probe from the vessel increases.

Just after the trough is captured by the wave probe, a crest emerges. This crest is related to the divergent wave, following the hollow. The height of the crest is seen to slightly vary from one probe to another. Yet, the differences are not considerable. Following the crest, another trough emerges. This trough is linked to the divergent waves. A different depth for this trough is recorded from one to another probe. The transverse location of the probe influences the depth of the trough. The turbulent behavior of the fluid is likely to be the reason for such a difference. The divergent wave is steep, and the air–water flow around the vessel is turbulent. This can stimulate the development of eddy viscosity in the direction of divergent waves, which generates shear stresses.

A second- and a third-wave crest are also recorded by each probe. These crests are seen to have smaller heights as time increases. This signifies that the divergent wave, recorded by a wave probe, is damped over time. The nonlinear behavior of the wave and the strong turbulence developed under the water surface can be the main reasons for the energy dissipation of the divergent wave. Following the divergent wave, the transverse wave is recorded by the probes. The phases of the transverse waves, recorded by the probes, are seen to be different. Transverse wave reaches the furthest probe first. From a top view, transverse waves propagate in a radial direction. Accordingly, the first probe records the transverse wave after all the other probes. The wave

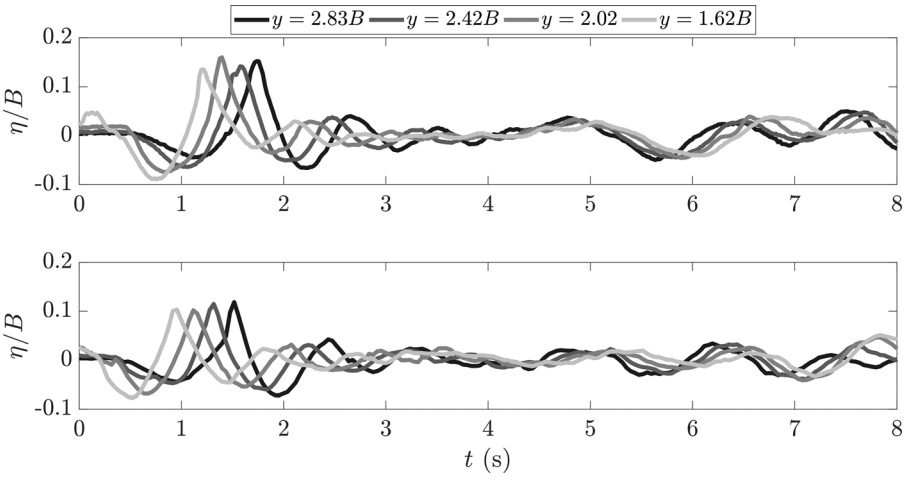

FIG. 7. Samples of the time histories of water surface elevation recorded by four different wave probes. The upper and lower panels show the data related to towing speeds of 4.0 and 7.0 m/s, corresponding to Froude numbers of 1.50 and 2.55.

heights of the transverse waves recorded by different wave probes are seen to be close to each other. There might be some differences, which are not significant. The height of the transverse wave will be reported later. The height of the divergent wave, recorded over three-period time, is seen not to be damped significantly. This implies that, unlike the divergent wave, the transverse waves, generated by the planing motion of a hard-chine boat, are less turbulent, and they tend to keep their energy for a longer distance.

The wake pattern is reconstructed using the recorded time histories. Time is converted into the space using $x = Ut$ (i.e., it is hypothesized that waves advance with a constant progressive speed, which equals the towing speed). The reconstructed wake patterns are presented in Fig. 8. Contours of the wake, generated by the planing motion of the vessel are plotted in this figure. Longitudinal and horizontal positions are normalized by using the beam of the vessel. As can be seen, the data are capable of reconstruction of the divergent wave. At the first probe, the crest of the longitudinal wave is set to be at a longitudinal position in between $5B$ and $6B$. The divergent wave is observed to have a smaller length for the case of higher towing speeds. In addition, the wake angle, the angle between the wave crest of the stationary divergent wave and longitudinal direction, is observed to decrease by the increase in towing speed. This fact agrees with previous physical observations, which were mentioned in Sec. I of the paper. The hollow, which is positioned behind the divergent wave, can

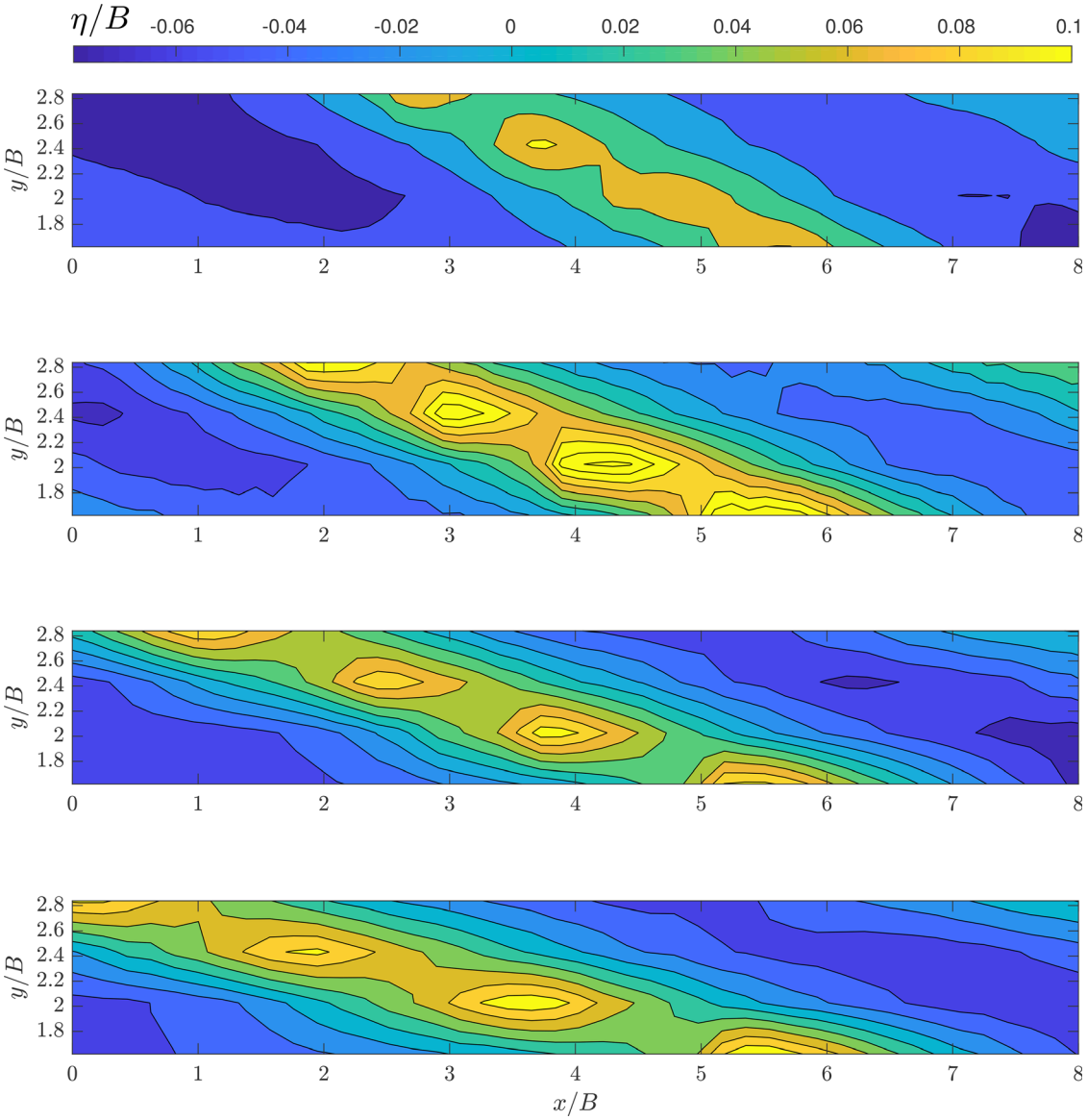

FIG. 8. Reconstruction of the wake pattern of the studied planing hull at four different towing speeds. Panels show the data corresponding to towing speeds of 4.0, 5.0, 6.0, and 7.0 m/s from the first to the fourth panel, respectively.

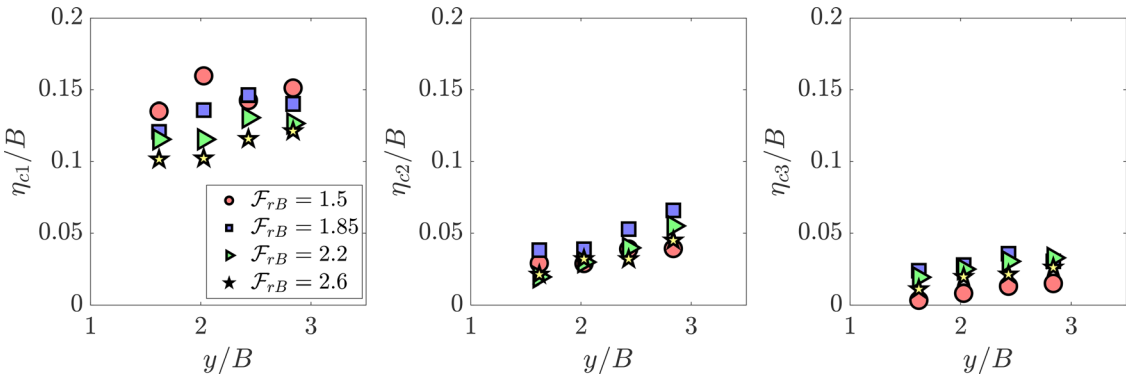

FIG. 9. Three wave crests of the divergent waves were recorded at each probe. The left, middle, and right panels, respectively, show the height of the first, second, and third wave crests. Circle, square, triangle, and star symbols, respectively, refer to data corresponding to beam Froude numbers of 1.50, 1.85, 2.20, and 2.60.

also be observed in the presented contours. For example, the hollow developing at the towing speed of 4.0 m/s, emerges at $6B < x < 7B$ at $y = 1.65B$.

The test procedures were carried out following the ITTC standard procedures for wave measurement and wave pattern resistance analysis (ITTC, 2021).

B. Divergent waves

Three first crests recorded of the divergent waves are found via measurements. The zero-crossing method, which is commonly used in physical oceanography, is applied to find the height of these crests (see more details of the zero crossing method in Thomson and Emery (1998). The heights of the crests are plotted in Fig. 9. The left, middle, and right panels correspond to the first, second, and third wave crests, respectively. At each panel, the height of the wave crest recorded by each probe is presented. In addition, the heights of the wave crests generated by all four towing speeds are presented in every panel. The wave crest and the transverse location of the wave probe are normalized using the beam of the vessel.

The first wave crest is seen to be higher at all towing speeds. The height of the first crest decreases by the increase in towing speed. This shows that the increase in towing speed leads to generations of smaller waves (lower wave steepness). The reductions of trim angle and sinkage of the vessel by the increase in towing speed explain this behavior. It can be seen that the height of the first wave crest increases as the distance between the wave probe and the vessel increases. For the case of the lowest towing speed, however, there is an exception. The height of the wave crest, recorded by the second wave probe, is greater than the height recorded by other probes.

The height of the second wave crest, corresponding to all probes and towing speeds, is much smaller compared to those of the first wave crest. It was previously observed that the height of the crest decreases over time (Fig. 7). Thus, this observation matches with the time history curves presented in Fig. 9. A substantial decrease in the height of the crest (from first to second) occurs for both the lowest and highest towing speeds. For the lowest towing speed, the first wave crest was larger than those of others and the wave steepness was very significant (compared to the wave steepness of the other towing speeds). The highest towing speed case generates strong turbulence field, which in turn attenuates the waves behind the vessel. The damping of the waves and the responsible mechanism leading to such damping will be discussed later.

The heights of the third wave crest of the divergent wave are seen to be smaller, compared to the second and the third crests. This implies that the energy of the divergent wave is still being damped. The smallest height of the wave crest is observed for the case of the smallest Froude number, which again implies that the significant energy damping occurs for the case of this towing speed. The largest height of the third wave crest is seen to occur for the case of the Froude number of 1.85. This implies that the smallest energy damping occurs at this towing speed.

The period of the divergent waves recorded at each probe is calculated. The instants with the same phases are found, and then, the time difference among them is calculated. The mean value is identified as the wave period. The calculated values of the wave periods are shown in Fig. 10. The scattered data refer to the corresponding value of each probe. The horizontal lines denote the average values of the period at each towing speed. As seen, the wave period might slightly vary from one probe to another. The probe that has the longest distance from the vessel has recorded a slightly smaller wave period compared to that of others. The average value of the wave period is seen to decrease by the increase in towing speed. At the lowest towing speed, corresponding to beam Froude number of 1.5, the recorded average period of the divergent wave is ~0.9 s. At the highest towing speed, the average period is approximately 0.86 s.

The damping of the height of the wave crest, wave amplitude, or depth of the through can be formulated as

$$\mathcal{X}(\mathrm{t} + \mathrm{nT}) = \mathcal{X}(\mathrm{t})\exp^{-\gamma(\mathrm{nT})}, \quad \mathrm{n} = 1, 2, 3, 4, \ldots. \tag{1}$$

In the above equation, $\mathcal{X}(\mathrm{t})$ is the value corresponding to the first wave. For example, it can be the height of the first wave crest. Here, n represents the number of the cycle. For example, $n = 2$ refers to the second wave crest. γ is the damping ratio of the parameter. As is seen, Eq. (1) is exponential. This means that the energy of waves is damped exponentially, which is very common in the case of surface waves. Wave amplitude includes both wave crest and trough. Therefore, the damping ratio corresponding to the wave amplitude is computed for all towing speeds. This coefficient is calculated using an exponential

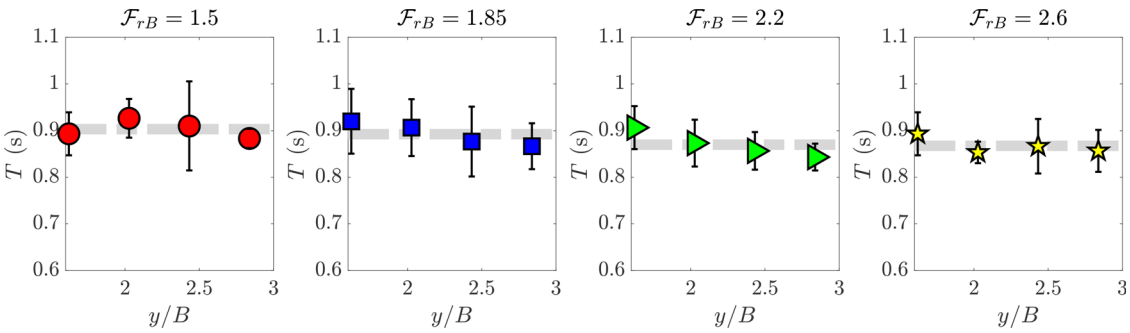

FIG. 10. Period of the divergent wave. The horizontal line refers to the average value of the period at each towing speed. Circle, square, triangle, and star symbols, respectively, refer to Froude numbers of 1.5, 1.85, 2.2, and 2.6.

fitting. The recorded wave amplitude and their corresponding periods were employed to establish the curve fitting.

The damping ratios found through curve fitting are displayed in Fig. 11. To analyze the data, damping ratios are normalized using the wave frequency ($f = 1/T$). The damping ratio varies across the probes. At all towing speeds, the probe that has the longest distance from the centerline has recorded the smallest value of the damping ratio. This physical observation, a smaller value of damping ratio that occurs at the last probe, is seen to be more significant for the case of two higher towing speeds, which are categorized in planing regimes. The mean value of the damping ratio of every towing speed is calculated. The horizontal lines show the mean values. It is evident from Fig. 11 that the mean value of the damping ratio of the highest speed is greater than those of all speeds. The second-largest value of the damping ratio is seen to occur at the smallest towing speed. This is consistent with the results, presented in Fig. 9. It was seen and also explained that the largest damping of the wave crest (and wave amplitude) occurs for the case of the highest towing speed.

The average value of the damping ratio of the Froude number of 2.2 is greater than that of the average value of the beam Froude number of 1.85. The damping ratio (gamma vs Fr_B) reaches a minimum value at beam Froude number of 1.85. This Froude number is identified in the semi-planing regime. It seems that the energy damping mechanism, causing the dissipation of the energy of the divergent wave, may depend on different physical phenomena in the planing and semi-planing regime. As discussed, the damping ratio decreases with the increase in towing speed in the semi-planing regime. This ratio increases by the increase in speed in the planing regime. This damping mechanism will be discussed later.

The energy damping of waves might occur by different mechanisms. First of all, the presence of cover on the sea, under which a boundary layer might develop, or the coupled fluid–solid waves might evolve, can cause the damping of the energy. In addition, the sea bottom can affect the energy of the wave in the case it is covered by mud or marine vegetation. Yet, these two mechanisms are irrelevant for the case of the present research. Note that, in the real sea with a deep water condition, the bottom is less likely to affect the water waves. However, near the beach, a muddy bottom [e.g., Almashan and Dalrymple (2015)] or a sea bed covered with marine vegetation (Paul *et al.*, 2012) may lead to energy dissipation. Waves propagating over such bottoms may be decayed exponentially. Yet, it does not occur in the present tests since the tank floor is not covered with any natural or artificial mud layer or marine vegetation. If the bottom can affect the water waves, the decay rate should be calculated and its effects on water waves need to be considered.

The nonlinear interaction of water waves with each other, or the breaking of the waves can also cause the damping of the energy. The breaking of the first crest of the divergent wave, which is the steepest wave, is not reported for fast boats and was not observed in experiments. The nonlinear interaction needs a longer distance for development. Furthermore, the energy dissipation caused by the nonlinear interaction between waves is not significant. The other mechanism

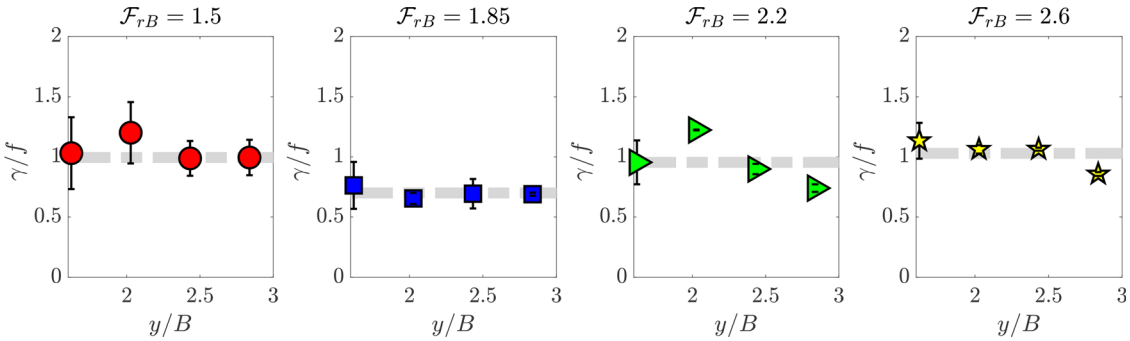

FIG. 11. Damping ratio of the divergent wave. The horizontal line refers to the average value of the damping ratio. Circle, square, triangle, and star symbols, respectively, refer to beam Froude numbers of 1.50, 1.85, 2.20, and 2.60.

that can result in energy dissipation is likely to be the turbulent development (Shomina *et al.*, 2020), which occurs in the lee of the vessel. It is more likely that the eddy viscosity, generated under the mixing of the flow layers dissipates the energy. Large shear stresses have been calculated in the direction of the propagation of the divergent waves in Hosseini *et al.* (2021). Therefore, the turbulent behavior of the fluid flow and its connection with the energy damping is analyzed in the present paper.

To understand the damping mechanism causing the attenuation of the divergent wave over time, the values of the damping ratio are plotted against Reynolds number. A greater Reynolds number leads to the generation of stronger turbulent flow. Also, for the case of fluid flow with a greater value of Reynolds number, more significant energy damping occurs. Yet, the Reynolds number can be computed in different ways. In the present research, two different Reynolds number s are employed. The first one is the Reynolds number of the waves, which is computed by using the orbital velocity of the wave as

$$\mathcal{R}_O = a^2 \omega \nu^{-1}. \tag{2}$$

Here, a is the amplitude of the wave, which is set to be the amplitude of the first recorded wave (i.e., the value of $\mathcal{A}_1$ is employed). ω is the wave frequency and ν is the kinematic viscosity of the water, which equals $10^{-6}\,\mathrm{m}^2/\mathrm{s}$ for the case of water. The other Reynolds number is defined by using the speed of the vessel and its length. This number is identified as the Reynolds number of the vessel, given by

$$\mathcal{R}_A = uL\nu^{-1}. \tag{3}$$

The damping ratio of the divergent wave is plotted against both Reynolds numbers. It is an indication of how the turbulent flow can lead to the damping of the energy. It is expected that the energy of damping ratio increases by the increase in Reynolds number. Therefore, the objective is to find the zones over which the damping ratio increases as a function of Reynolds number. The scattered data are shown in Fig. 12. The left and right panels, respectively, show γ/f vs $\mathcal{R}_O$ and γ/f vs $\mathcal{R}_A$ curves. Note that the damping ratio is normalized using the wave frequency of the divergent wave (Fig. 10).

Based on the definition adopted for the Reynolds number of waves, the divergent wave decreases by the increase in Froude number in semi-planing regime. This is due to the typical behavior of the high-speed planing hull where the amplitude of the generated wave decreases with the increase in the towing speed. The reduction of the wave amplitude is mainly related to the reduction of the dynamic trim and sinkage, though the towing speed increases in the fully planing regime. Furthermore, the steepness of the waves decreases by the increase in towing speed, and thus, the Reynolds number of waves decreases by the increase in Froude number. The Reynolds number of the vessel grows with towing speed. A vertical line is plotted in both panels. This vertical line demonstrates the limit of the planing regime. In the left panel, the data, scattered on the left side of this line, refer to the ones observed in the planing regime. However, in the right panel, the data, scattered on the right side of this line, refer to the ones corresponding to the planing mode. Overall, it is expected that large Reynolds number results in larger energy dissipation. The positive slope for γ/f vs $\mathcal{R}_O$ is seen to occur in the semi-planing regime. In contrast, the positive slope for γ/f vs $\mathcal{R}_A$ data is observed in the planing regime. This observation implies that the damping ratio of the divergent wave is dependent on the Reynolds number of the wave in the semi-planing regime, but it is a function of the Reynolds number of the vessel in the planing regime. It seems that, when the vessel advances in fully planing condition ($Fr_B > 2$), the eddies emerging behind the vessel dissipate the energy of divergent waves. However, for the case of lower towing speeds (semi-planing regime), the wave-induced turbulence is leading to energy damping. The reason for this behavior will be explained later.

The wake angle, the angle between the divergent wave, and the velocity of the vessel are measured by using the data. The related data are presented in Fig. 13 (filled markers). As can be seen, the data diverge from the Kelvin Wake angle (which is indicated with the dashed horizontal line). To provide a better understanding of the effects of Froude number on the wake angle, the previous experimental data of Moisy and Rabaud (2014a) are also plotted in Fig. 13 (unfilled markers). A cylinder with a diameter of $\mathcal{D}$ was towed in their experiments. Physically, no rooster tail emerges and no flow separation occurs for a towed cylinder, though the effects of towing speed on the wake angle could be observed. Moisy and Rabaud (2014a) performed the tests for cylinders with different diameters, which are distinguished from each other by bond number, given by

$$\mathcal{B}_o = \frac{\mathcal{D}}{\lambda_c}, \tag{4}$$

where λ_c is 16.3 mm.

As seen, our observation fits with the data measured in the experimental study of Moisy and Rabaud (2014a). The wake angle, measured in our experiments, decreases by the increase in Froude number.

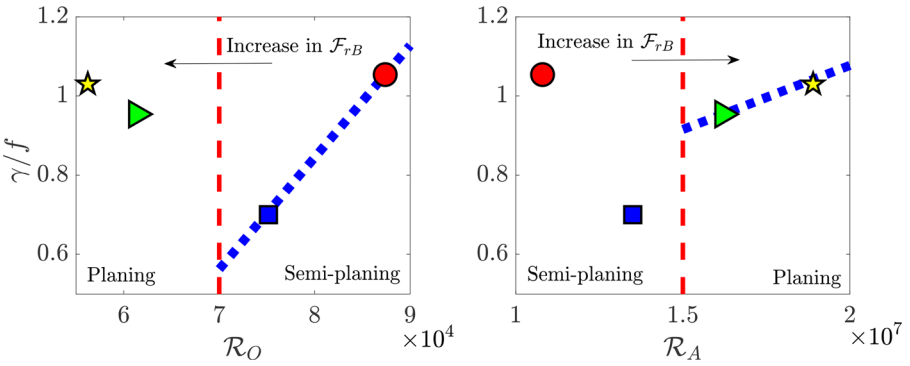

FIG. 12. Damping ratio of the divergent wave. The left panel shows the γ/f vs $\mathcal{R}_O$ data. The right panel shows the γ/f vs $\mathcal{R}_A$ data. The vertical line shows the limit of the planing regime in both panels. Circle, square, triangle, and star symbols, respectively, refer to the data corresponding to Froude numbers of 1.5, 1.85, 2.2, and 2.6.

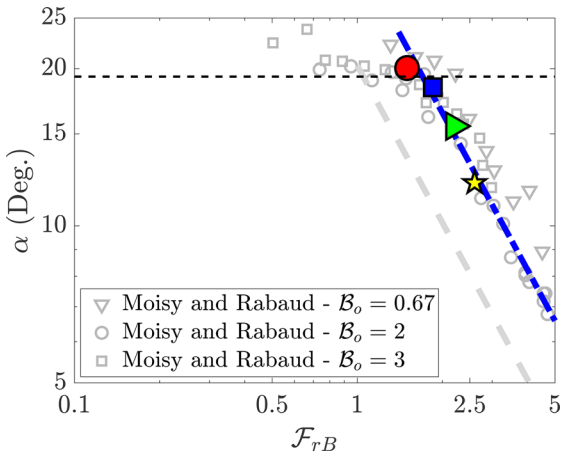

FIG. 13. Wake angle (filled markers) as a function of Froude number. The black dashed line shows the Kelvin wake angle, which is constant over all Froude numbers. The dashed gray curve shows the $\propto$ vs Fr_B plots constructed with Eq. (5). The dashed–dotted blue curve shows the $\propto$ vs Fr_B plots constructed with Eq. (6). Note that the vertical and horizontal axes are shown on a logarithmic scale. Circle, square, triangle, and star symbols, respectively, refer to the data corresponding to beam Froude numbers of 1.5, 1.85, 2.2, and 2.6. The experimental data measured by Moisy and Rabaud are also presented in this figure (unfilled markers).

Similarly, the data measured by Moisy and Rabaud (2014a) are seen to decrease under the increase in Froude number as this number goes beyond a specific limit, which is seen to be greater for the smallest value of bond number ($\mathcal{B}_o = 0.67$). This provides evidence that the scale can influence the wake angle. The wake angle of a body with a smaller dimension may diverge from the Kelvin angle at a greater Froude number. Note that the bond number reflects the importance of the gravity force compared to surface tension forces. A great value of this number indicates that waves are less likely to be influenced by the surface tension forces. Note that for the present tests, bond number is 163.

The vertical and horizontal axes of Fig. 13 are presented in logarithm scales, which helps us understand the way the wake angle decreases by the increase in Froude number. Wake angle measured in the present tests is seen to follow a $Fr_B^{-1.0}$ curve. This well matches with the previous theoretical model developed by Rabaud and Moisy (2013). Based on their developed model, the wake angle of relatively large beam Froude numbers can be approximated by

$$\propto = \frac{1}{2\sqrt{2\pi} Fr_B \sqrt{B/L_{WL}}}. \tag{5}$$

The $\propto$ vs Fr_B curve (dashed gray curve), that is, constructed by Eq. (5) is plotted in Fig. 13. The slope of the wake angles measured in the previous research and that of predictions made by Eq. (5) are similar. Yet, the experimental data do not match with the curve constructed by Eq. (5). One possible reason for this difference is the planing motion, which gives rise to hydrodynamic force, affecting the pressure distribution acting on the bottom surface of the boat. The other possible reason can be the turbulent rooster tail generated behind the boat, which is not developed behind a ship. Note that Eq. (5) does not consider any of the aforementioned phenomena. Using a least squares method, the wake angle as a function of beam Froude number can be formulated as

$$\propto = \frac{1}{0.61\left(2\sqrt{2\pi} Fr_B \sqrt{B/L_{WL}}\right)} \approx \frac{1}{3 Fr_B \sqrt{B/L_{WL}}}. \tag{6}$$

Note that Eq. (6) is formulated for large Froude number. A blue line indicating the $\propto$ vs Fr_B curve constructed using Eq. (6) is plotted in Fig. 13. Interestingly, the curve constructed using the suggested equation matches with those experimental data of Moisy and Rabaud (2014a) corresponding to bond numbers of 2 and 3. Yet, the results corresponding to the lowest bond number diverge from the curve constructed using the suggested equation. This can be due to the effects of surface tension forces that can affect the fluid motion generated by the body towed with a low bond number.

As the Froude number of the vessel goes beyond 2.0, the wake angle becomes smaller than 16°. In this condition, the wake pattern is much narrower compared to what happens in a semi-planing regime. Compared to the semi-planing regime, divergent waves, thus, are much closer to the centerline and they are affected by the eddies generated behind the vessel operating in a planing regime. Thus, the turbulence flow developed around the vessel can decay the energy of divergent waves more significantly. This matches with the observations made in Fig. 12. It was explained that when towing speed increases, the eddies generated by the advancement of the vessel are more likely to cause the energy damping of the divergent waves. The results of Fig. 13 substantiate this observation. The wake angle is small, and thus, divergent waves are propagating in a direction, that is, closer to the center lines. Thus, they are more affected by the eddies, generated in the lee of the vessel, when the vessel advances with a Froude number greater than 2.0. It is worthy to note that the eddy length is seen to vary from 0.014B to 0.14B in the very recent numerical simulations of Hosseini *et al.* (2021).

C. Transverse waves

As it was seen in Fig. 7, transverse waves are recorded by all probes during the tests. Following the divergent waves, a transverse wave propagates. The periods of transverse waves, as it will be shown later, are relatively long compared to those of divergent waves. To identify transverse waves, the water surface elevation related to the divergent wave is excluded from the recorded time histories. Note that both divergent and transverse waves are propagating in deep water conditions. Furthermore, the superposition law can be used. The extraction of the time history of the transverse waves from the recorded time history for both waves is performed by

$$\eta_t(t) = \eta(t) - \eta_d(t) - \eta_{d-cutt}(t). \tag{7}$$

Here, $\eta_d(t)$ is the water surface elevation corresponding to divergent waves, which is formulated by using an airy theory, as per

$$\eta_d(t) = \mathcal{A}_1(e^{-\gamma t})(\cos(\omega t)). \tag{8}$$

η_{d-cut} is the waves reflected by the right and left walls that may meet the transverse wave at X_{cut}/u, given by

$$\eta_{d-cut}(t) = \mathcal{A}_1\left(e^{-\gamma\left(t+\frac{X_{cut}}{u}\right)}\right)(\cos(\omega(t + X_{cut}/u)). \tag{9}$$

X_{cut} is the wave-cut distance and can be calculated by using the beam of the basin and the wake angle. More clarification of the wave-cut distance can be found in ITTC (2021). Note that free surface elevation of

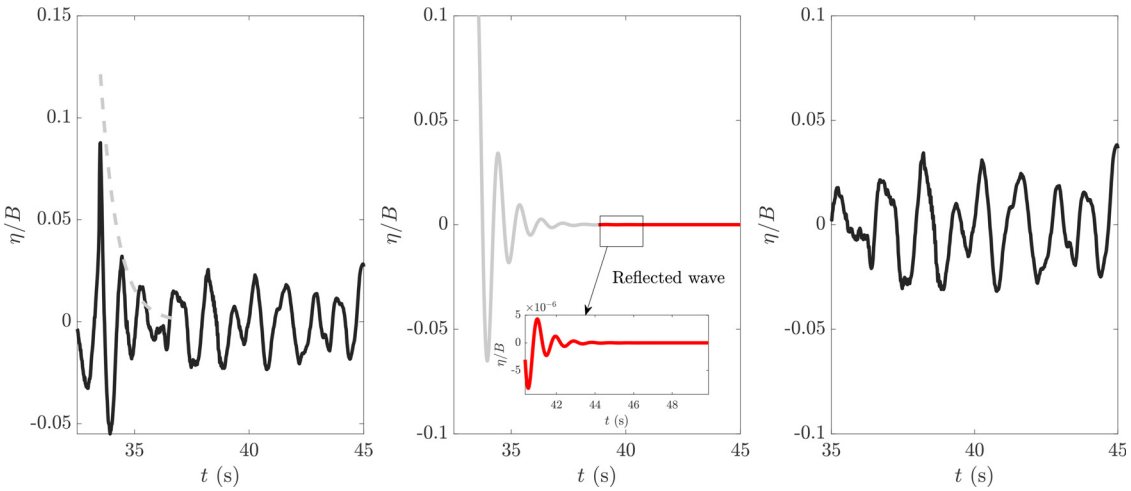

FIG. 14. Extraction of the transverse wave from the water surface elevation. The red plot in the middle panel indicates the reflected waves. A close-up view of the reflected wave is also shown in this panel.

$\eta_{d-cut}(t)$ is very scant as divergent waves are damped with a very high rate as explained before.

Figure 14 shows an example of the water surface elevation of the transverse wave, which is extracted through the above formulations. As seen, the transverse wave shows a nonlinear behavior, which is investigated later. Wave–wave interaction is likely to occur.

The mean value of the period of the transverse waves is computed at each probe and presented in Fig. 15. As seen, the period might slightly differ from one probe to another. Less difference between the recorded periods at each probe can be seen for the case of two higher towing speeds, both of which are categorized in the planing regime. The average value of the period, corresponding to each towing speed, is also computed. The average values are shown with horizontal lines. The period of a transverse wave is longer than 1.0 s at all towing speeds. This signifies that the transverse wave advances with a longer period. The period is seen to slightly decrease by the increase in towing speed. The decrease in the period is not very significant.

The wavelength of the transverse wave is calculated using the measured wave period and the speed of the vessel. The product of the wave period and the towing speed is computed and is defined to be the wavelength of transverse wave. Results are plotted in Fig. 16. The wavelength, again, is seen to slightly vary from one probe to another. It is seen that a higher towing speed results in a longer wavelength. The average value of the wavelength is also computed for all towing speeds. Horizontal lines show the average values of the wavelength of each towing speed.

The wavelength against the wave period of the transverse waves is displayed in Fig. 17. The results are compared against the linear theory. The dispersion relationship of the deep-water waves is used, which gives a wavelength of $\lambda = 2\pi u^2 g^{-1}$. As seen, the wavelength measured through towing tank experiments deviates from the theory. With the increase in the speed of the vessel, the experimental value of the wavelength diverges more remarkably from the λ/B vs Fr_B plot. The results presented in Fig. 17 confirm that transverse waves do not obey the linear theory. They are strongly nonlinear. Wave–wave interaction, as mentioned earlier, might emerge as the transverse waves develop. This might be the possible reason for this observation. Here, it is worthy to note that the tank depth is 4.25 m, ensuring that waves do not develop in a shallow water condition (i.e., the ratio wavelength over the water depth is greater than 1/20).

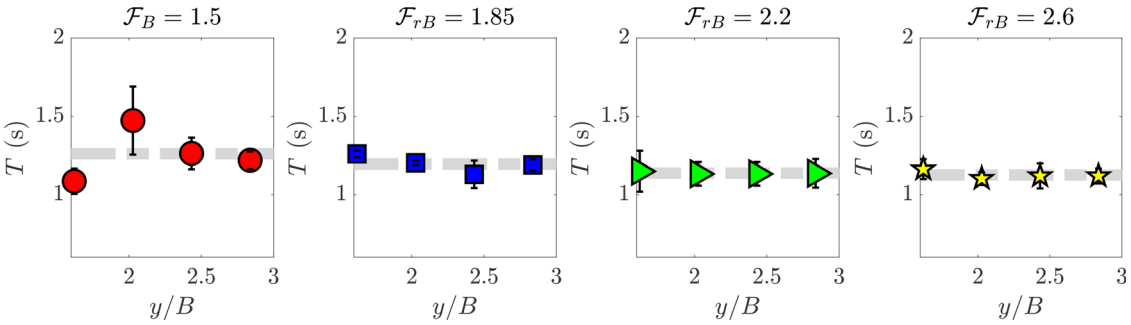

FIG. 15. The wave period of the transverse waves observed in measurements. The horizontal line refers to the average value of the wavelength. Circle, square, triangle, and star symbols, respectively, refer to the data corresponding to beam Froude numbers of 1.5, 1.85, 2.2, and 2.6.

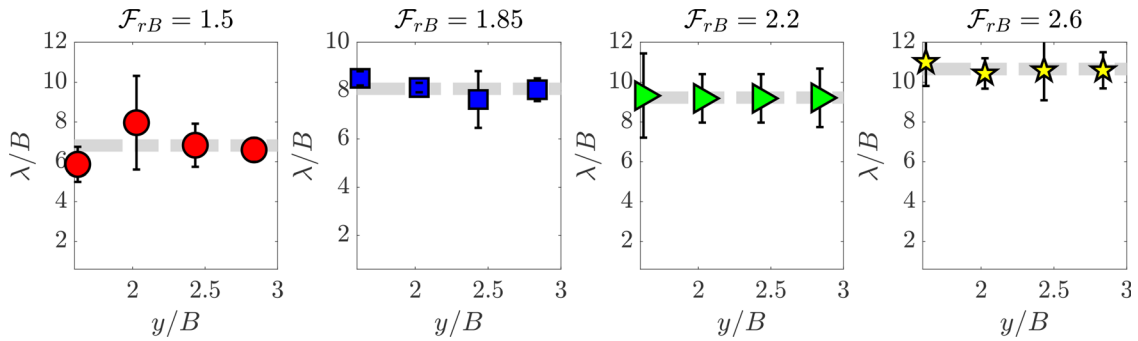

FIG. 16. The wavelength of the transverse waves observed in measurements. The horizontal line refers to the average value of the wavelength. Circle, square, triangle, and star symbols, respectively, refer to the data corresponding to beam Froude numbers of 1.5, 1.85, 2.2, and 2.6.

The energy spectrum of the transverse wave is calculated by using fast Fourier transform (FFT). It assists us to understand the development of the nonlinear interaction between water waves. This interaction occurs in the case the energy of waves is transferred from the carrier period to other ones. This might be more significant as the waves travel a longer distance. For the case of the present research, nonlinear interaction is expected to be larger for the case of the furthest wave probe. Note that to perform the analysis, divergent waves are excluded from the time history and transverse waves are included. The energy of divergent waves is decayed exponentially. Yet, the energy of transverse waves is not reduced significantly. This can be seen in the left panel of Fig. 14 in which the time history curve of a transverse wave is shown.

Figure 18 illustrates the computed energy spectra of the transverse waves. The first, second, third, and fourth columns, respectively, show the energy spectra of the waves recorded at probes 1, 2, 3, and 4. The first, second, third, and fourth rows, respectively, show the energy spectra corresponding to Froude numbers of 1.5, 1.85, 2.2, and 2.6. The vertical and horizontal axis, respectively, show the energy spectrum and the frequency. The energy spectrum is normalized by using the maximum value of the energy spectrum. Angular frequency is normalized by using the value of peak frequency.

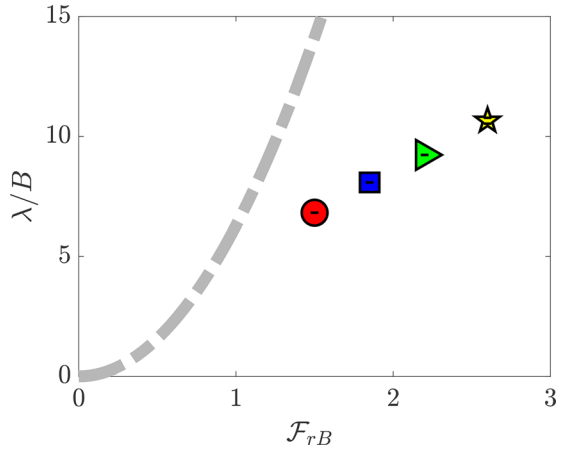

FIG. 17. The wavelength of the transverse wave as a function of beam Froude number. The reported data are the average value of wavelength measured at each probe. The plotted curve is the $\lambda/B = 2\pi u^2 g^{-1}/B$ plot.

As is apparent, the computed energy spectra show nonlinear behavior in most of the cases. Energy is concentrated at the peak frequency. Yet, it is partially distributed over the other frequencies. The energy distributed over the frequencies, which are smaller than the peak frequency, is larger compared to the energy distributed at frequencies that are greater than the peak frequency. This implies that energy is more prone to be shifted to longer periods. This observation fits with the physics of the surface waves.

The energy spectrum of the transverse wave is seen to vary from one wave probe to another probe. This means that nonlinear effects on wave energy vary spatially. Such behavior is common to occur when surface waves are nonlinear. Examples can be seen in the cases rogue waves are generated in wave tanks/basins (Ma *et al.*, 2012). At the second considered towing speed, the energy spectrum slightly differs from one probe to another. This signifies that, while nonlinearity is developed, its effects on the wave energy are not very significant. Interestingly, at the two larger towing speeds, nonlinearities are observed to considerably affect the energy spectrum. The energy spectra of the closest probe to the vessel are highly narrow at these two towing speeds. Yet, the energy spectra of the farthest probe from the vessel are seen to be modulated more remarkably. A significant amount of energy is transferred to lower frequencies.

Overall, two points can be concluded. First, the transverse waves generated by the motion of a hard-chine boat advancing in a semi-planing or planing regime are strongly nonlinear. Waves can be more nonlinear in the case where the speed of the vessel is higher. This might be due to the generation of the transom waves behind the vessel. As explained earlier, water is separated from the transom of the vessel, leading to large turbulent kinetic energy in the lee of the vessel. This can affect the development of the transverse wave. Turbulent flow makes the problem strongly nonlinear. For the case of a free-run test with a higher towing speed, the turbulent flow behind the vessel is stronger, so the nonlinearity of the waves increases. It is worth noting that theoretical observation for the development of nonlinearity in the wake of high-speed ships is documented by Pethiyagoda *et al.* (2017). In addition, the nonlinearity of the transverse waves implies that other frequencies may involve, which increases the risk of shoreline erosion.

To investigate the physics of the transverse wave and the underlying reason behind the nonlinearities, two other characteristics of the

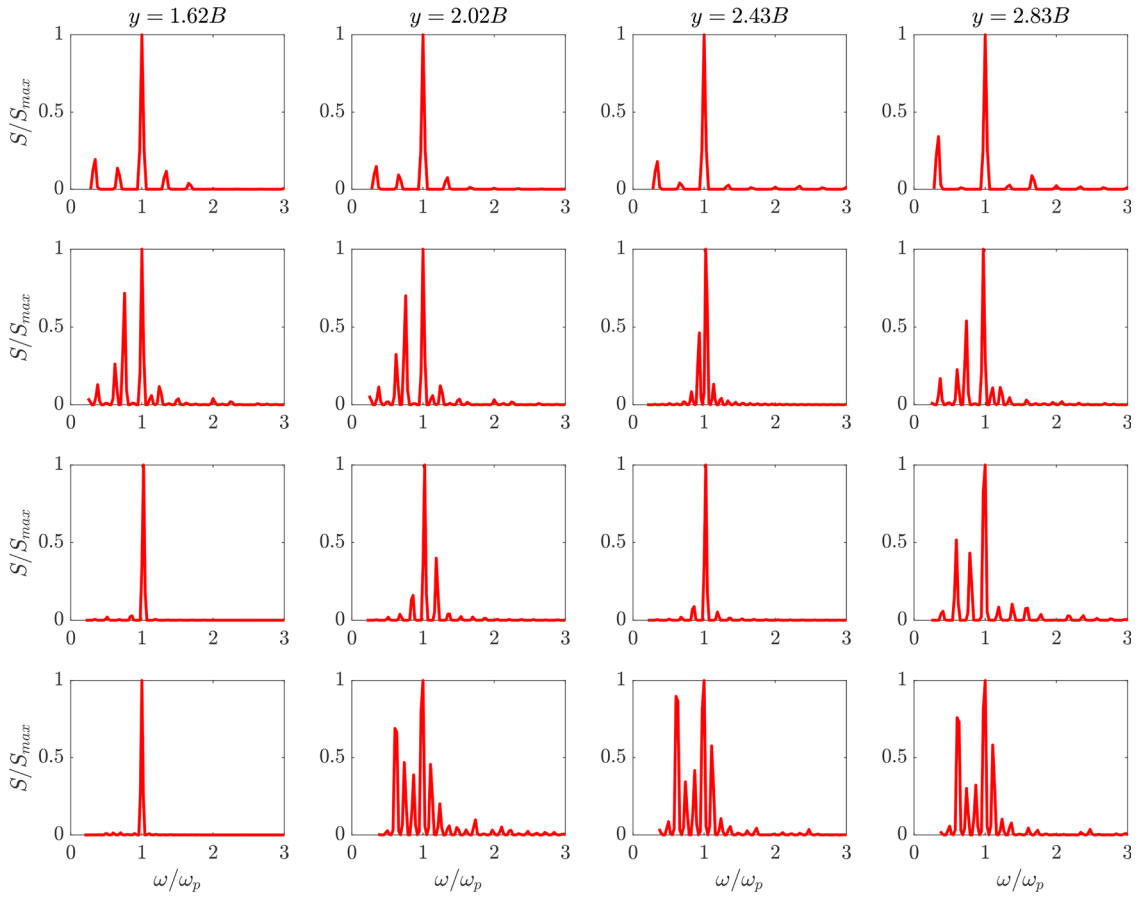

FIG. 18. Energy spectra of the transverse waves were recorded at different wave probes. The first, second, third, and fourth columns, respectively, show the results corresponding to the waves recorded at y = 1.6B, 2B, 2.4B, and 2.8B. The first, second, third, and fourth columns, respectively, show the data corresponding to the beam Froude numbers of 1.5, 1.85, 2.2, and 2.6.

transverse waves are also found through measurements. The first parameter is the wave height of the transverse wave, and the second one is the kurtosis of the water surface elevation, recorded at each probe.

The values of significant wave height and kurtosis are presented in Fig. 19. The first row shows the height of the waves, and the second row shows the values of kurtosis. For the case of the wave height, the average value of the height is also presented (horizontal lines). Wave height is observed to be slightly dependent on the transverse position of the wave height. At the lowest towing speed and highest towing speed, a slightly smaller wave height is recorded at the farthest wave probe. For the case of the highest towing speed, flow is strongly turbulent and can partially dissipate the energy of the waves. The mean value of the wave height is observed to decrease by the increase in towing speed. As the towing speed increases, the average value of the wave height is seen to converge to 0.06B.

The values of kurtosis are observed to be over 1.8 in all cases. This implies that transverse water waves, recorded at each probe, are nonlinear and non-Gaussian. Kurtosis might vary spatially. The larges value of kurtosis is observed at the first wave probe. The interesting point is that the value of kurtosis never gets smaller than 1.8. In general, the values of the kurtosis confirm that transverse waves are nonlinear, and the shift of energy from the carrier frequency to the other frequencies is possible.

The *p.d.f* (probability density function) plots of the recorded water surface elevations are presented in Fig. 20. Also, the Gaussian distribution curves are presented in this figure. At each panel, the *p.d.f* plots of the recorded surface elevations at each probe are shown.

The presented graphs demonstrate that recorded waves at each probe can be non-Gaussian. The *p.d.f* computed for the two higher towing speeds are seen to deviate more from the Gaussian probability distribution. The *p.d.f* graphs diverge from the Gaussian probability distribution at two lower towing speeds as well. Yet, the deviation is significant for the case of two larges Froude numbers as mentioned. This is consistent with observations made in Fig. 19. It was reported that the nonlinearity is stronger at higher towing speeds.

Finally, it is worthy to note that the tests carried out in the present research correspond to a planing model with a length of 2.61 m. Results can be scaled to those of an actual scale through the Froude scaling law. The beam Froude number should be used as the wetted length of a planing hull reduces by the increase in speed and is not suggested to be used for scaling the results of the model to that of a real boat [see, e.g., Fridsma (1969)].

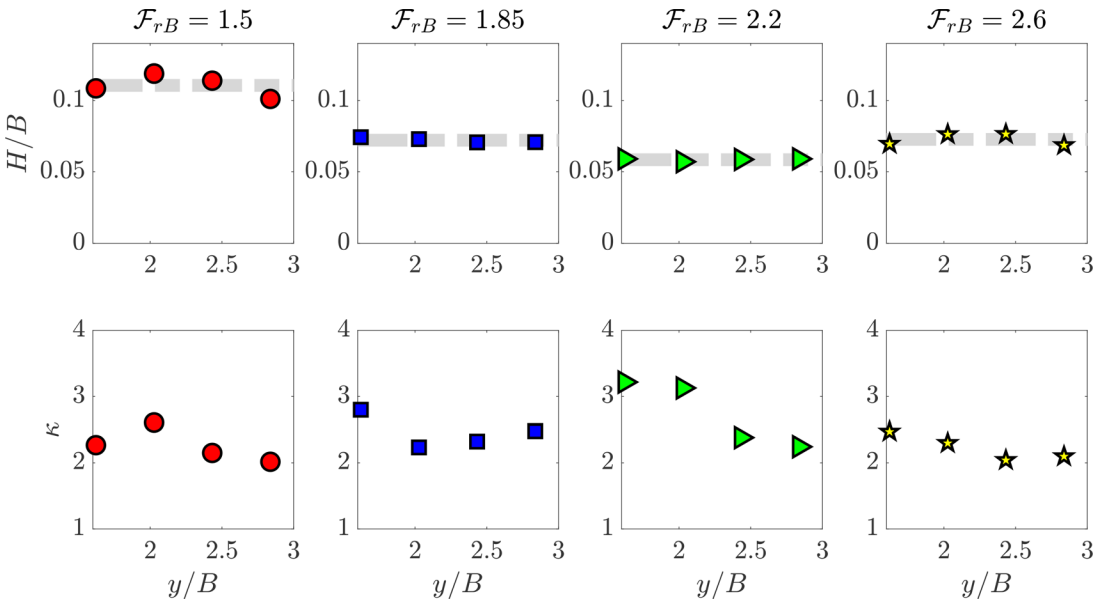

FIG. 19. Significant wave height (upper row) and kurtosis (lower row) values of the transverse waves. Circle, square, triangle and star symbols, respectively, refer to the data corresponding to beam Froude numbers of 1.5, 1.85, 2.2, and 2.6.

Except the wave period, all different properties of waves were presented in a non-dimensional. Wave period can be normalized by using $\sqrt{B/g}$ or B/u, the latter of which considers the effects of speed of the boat (towing speed). Tests for different scales need to be carried out to evaluate how the wave period can be normalized, and how the scale can affect the results. The previous results of Moisy and Rabaud (2014a), however, have provided an early understanding of the scale effects on wake angle, as was shown in Fig. 13. All in all, it should be mentioned that the scalability of the results and the scale effects are out of the scope of the present research and were not deeply studied in this paper. They are recommended to be studied in the future. Yet, readers who are interested to know more about the scaling of the wake data are referred to Moisy and Rabaud (2014b).

IV. CONCLUSIONS

In the present paper, the wake waves of a high-speed boat operating in planing mode were analyzed by using experimental measurements in the towing tank of the University of Naples Federico II. This paper was aimed at improving the understanding of the wake waves of a high-speed planing vessel by analyzing the time history of the waves recorded by four different wave probes. The wake waves were seen to emerge in the lee of the vessel. The water, that is, separated from the dried transom of the lifting surface, leads to a noticeable disturbance in water surface elevation and pressure, just behind the stern, which is known as rooster tail. Just behind the rooster tail, two waves, including the divergent and transom waves, are generated. Both divergent and

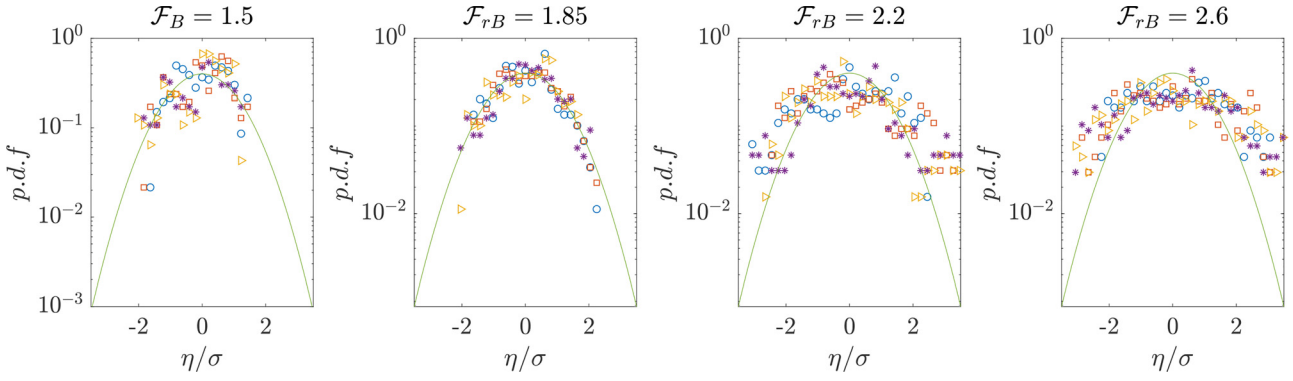

FIG. 20. *p.d.f.* plots of water surface elevations produced by transverse waves. Circle, square, triangle, and asterisk symbols respectably show the data corresponding to the recorded water surface elevations at y = 1.6B, 2B, 2.4B, and 2.8B.

transverse waves were identified through measurement, and their temporal evaluation was analyzed.

Divergent waves were seen to last over three cycles at each probe. Three wave crests and three-wave troughs were observed. The corresponding wave period was seen to decrease by the increase in the Froude number of the vessel. The first wave height and first wave amplitude were seen to decrease by the increase in towing speed. Divergent waves were seen to damp over time. The damping that occurs is the main reason that the divergent wave vanishes after three periods of time. The damping of the divergent wave was seen to be significant for the case of the highest and lowest Fr_B. The lowest Fr_B is 1.5 (semi-planing), and the highest is 2.6 (full planing). The mechanism that causes damping was investigated. The turbulent fluid motion was hypothesized to be the main contributor to the energy damping of the divergent waves. Two Reynolds numbers were identified: (1) wave-induced Reynolds number, and (2) Reynolds number of the vessel. The damping ratio was plotted vs both of these Reynolds numbers. It was seen that the damping ratio increases by the increase in wave-induced Reynolds number in the semi-planing regime, while it increases by the increase in Reynolds number of the vessel in the planing regime. The wake angle, the angle of the wake wedge in a stationary plane, was also found through measurements. Wake angle was seen to decrease by the increase in towing speed, and to be proportional to $Fr_B^{-1.0}$.

Wake angle was observed to be lower than 15° in the planing regime. This implied that the divergent waves may be more dependent on the turbulent flow, emerging behind the vessel in the planing regime, compared to the semi-planing regime. This is likely to be the reason for what was observed for the damping ratio of the divergent waves vs Reynolds number of the vessel in planing mode.

Transverse waves were extracted from the water surface elevation recorded by wave probe. The divergent wave was formulated by using the Airy theory, and the damping ratio of the divergent wave was employed to exclude the divergent waves from the recorded water wave. The wave period of the transverse waves was seen to be longer compared to that of divergent waves. This period was seen to slightly decrease by the increase in towing speed. The height of the transverse wave was observed to decrease by the increase in towing speed. Spectral analysis of the transverse wave was performed. The energy of the transverse wave was seen to be distributed over different frequencies. The energy spectra curves were seen to be changed from the closest probe to the vessel to the farthest one. The energy spectra of transverse wave were seen to be distributed over a wider range of frequency for the case of two higher towing speed values, both of which are categorized in the planing regime. This implied that transverse waves may get highly nonlinear by the increase in speed in the planing regime. The kurtosis number of the transverse waves was computed, and it was found to be over 1.8 in all the cases. This confirmed that transverse waves propagating in the lee of a planing hull are strongly nonlinear. The *p.d.f* plots of water surface elevations generated by the transverse waves were presented. It was observed that waves are non-Gaussian at all four towing speeds. The deviation of the experimental data from the Gaussian distribution function was seen to be more significant for the case of two higher towing speeds, which are identified in planing mode.

The experimental analysis performed in the present research provides a meaningful and useful understanding of the planing wake waves. These waves are generated in the lee of the transom of the vessel, where the boat has left a strong turbulent flow. Overall, it was observed that the pressure variation on the water surface downstream, where flow is strongly turbulent, may affect the wake waves generated by the planing vessel. The divergent waves may propagate with a larger angle, which, in turn, decreases the wake angle. Divergent waves are temporally damped at a very large rate. Yet, the set of transverse waves propagating in the direction of the disturbance was seen to be strongly nonlinear and their energy was observed to be concentrated over different frequencies. The shift of energy toward smaller frequencies was seen to be significant. This implies that the heavy traffic of high-speed planing hulls in inland waterways and coastal seas can lead to a significant amount of energy of waves, related to transverse waves, which propagates with relatively high speed. The early understanding of the problem was formed in the present research. However, the problem needs to be investigated in more detail in the future. As an outlook of future studies, field observations are needed to be performed to identify the wake of high-speed planing hulls in real conditions. In addition, the shallow water planing problem, which can lead to the generation of strong nonlinear wakes waves, is recommended to be studied.

ACKNOWLEDGMENTS

S.T. and P.S. are both supported by Melbourne Research Scholarship, awarded by the University of Melbourne. F.D.C. has been supported with "Progetto di ricerca di rilevante interesse nazionale; Bando PRIN 2017-Progetto 2017X7Z8S3."

AUTHOR DECLARATIONS

Conflict of Interest

The authors declare that there is no conflict of interest.

DATA AVAILABILITY

The data that support the findings of this study are available from the corresponding author upon reasonable request.

APPENDIX: CALM-WATER PERFORMANCE OF THE MODEL

Calm-water performance tests of the boat have been performed in 2016. The vessel was towed at different towing speeds, and its motions in vertical direction were recorded and presented in De Luca and Pensa (2017). The boat was observed to reach steady heave and pitch displacements. The former is the CG rise-up, and the latter is the dynamic trim angle. In this appendix, the trim angle vs beam Froude number (left panel of Fig. 21) and CG rise-up vs beam Froude (right panel of Fig. 21) curves are re-presented. Trim angle reaches a peak value at Froude numbers of 1.85. CG rise-up monotonically increases under the increase in the towing speed. Readers interested in the calm water test are referred to De Luca and Pensa (2017). Also, wave-induced tests of this hull were performed recently. Results of those tests are presented in Tavakoli *et al.* (2020).

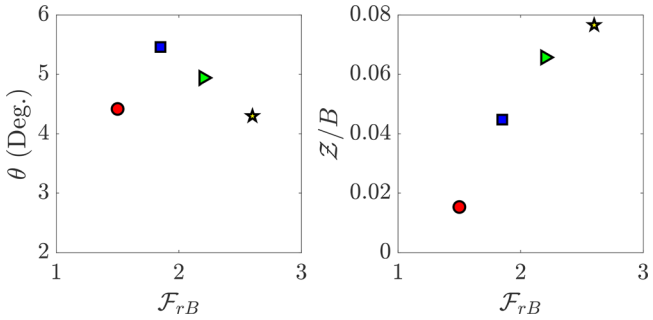

FIG. 21. Dynamic trim angle (left) and CG rise-up (right) of the boat. Data are measured through calm water tests and were previously presented by De Luca and Pensa (2017).

REFERENCES

Almashan, N., and Dalrymple, R. A., "Damping of waves propagating over a muddy bottom in deep water: Experiment and theory," Coastal Eng. **105**, 36–46 (2015).

Bauer, B. O., Lorang, M. S., and Sherman, D. J., "Estimating boat-wake-induced levee erosion using sediment suspension measurements," J. Waterw. Port Coastal Ocean Eng. **128**, 152–162 (2002).

Begovic, E., Benassai, G., Nocerino, E., and Scamardella, A., "Field investigation of wake wash generated by HSC in the Bay of Naples," in *Proceedings of the 2nd International Conference on Marine Research and Transportation* (University of Naples "Federico II," 2007), pp. 243–252.

Benassai, G., Piscopo, V., and Scamardella, A., "Field study on waves produced by HSC for coastal management," Ocean Coastal Manage. **82**, 138–145 (2013).

Benassai, G., Piscopo, V., and Scamardella, A., "Spectral analysis of waves produced by HSC for coastal management," J. Mar. Sci. Technol. **20**, 417–428 (2015).

Bilkovic, D., Mitchell, M., Davis, J., Andrews, E., King, A., Mason, P., Herman, J., Tahvildari, N., and Davis, J., "Review of boat wake wave impacts on shoreline erosion and potential solutions for the Chesapeake Bay," Report No. 17-002 (STAC Publication, Edgewater, MD, 2017), p. 68.

Bilkovic, D., Mitchell, M., Davis, J., Herman, J., Andrews, E., King, A., Mason, P., Tahvildari, N., Davis, J., and Dixon, R. L., "Defining boat wake impacts on shoreline stability toward management and policy solutions," Ocean Coastal Manage. **182**, 104945 (2019).

Caplier, C., Rousseaux, G., Calluaud, D., and David, L., "Energy distribution in shallow water ship wakes from a spectral analysis of the wave field," Phys. Fluids **28**, 107104 (2016).

Chung, Y. K., and Chun, H. H., "High-speed theory for the planing of a flat plate at high Froude number," Ocean Eng. **34**(11–12), 1552–1560 (2007).

Colen, J., and Kolomeisky, E., "Kelvin–Froude wake patterns of a traveling pressure disturbance," Eur. J. Mech. -B/Fluids **85**, 400–412 (2021).

Cumberbatch, E., "Two-dimensional planing at high Froude number," J. Fluid Mech. **4**(5), 466–478 (1958).

Darmon, A., Benzaquen, M., and Raphaël, E., "Kelvin wake pattern at large Froude numbers," J. Fluid Mech. **738**, R3 (2014).

Darrigol, O., *Worlds of Flow: A History of Hydrodynamics from the Bernoullis to Prandtl* (Oxford University, Oxford, 2005).

De Luca, F., Mancini, S., Miranda, S., and Pensa, C., "An extended verification and validation study of CFD simulations for planing hulls," J. Ship Res. **60**, 101–118 (2016).

De Luca, F., and Pensa, C., "The Naples warped hard chine hulls systematic series," Ocean Eng. **139**, 205–236 (2017).

Doctors, J., "Hydrodynamic of the flow behind a transom stern," in Proceedings of the 29th Israel Conference on Mechanical Engineering, Haifa (2003).

Eeltink, D., Lemoine, A., Branger, H., Kimmoun, O., Kharif, C., Carter, J., Chabchoub, A., Brunetti, M., and Kasparian, J., "Spectral up- and downshifting of Akhmediev breathers under wind forcing," Phys. Fluids **29**(10), 107103 (2017).

Faltinsen, O. M., *Hydrodynamics of High-Speed Marine Vehicles* (Cambridge University Press, 2005).

Faltinsen, O. M., and Zhao, R., "Numerical predictions of ship motions at high forward speed," Philos. Trans. R. Soc. London, Ser. A **334**, 241–252 (1991).

Fridsma, G., "A systematic study of the rough-water performance of planing boats," Report No. R-1275 (Davidson Laboratory, Stevens Institute of Technology, Hoboken, NJ, 1969), p. R1275.

Garland, W. R., and Maki, K. J. A., "Numerical study of a two-dimensional stepped planing surface," J. Ship Prod. Des. **28**(2), 60–72 (2012).

Ghadimi, P., Dashtimanesh, A., Zamanian, R., Chekab, M. A. F., and Mirhosseini, S. H. R., "Rooster tail depression by originating a modified transom stern form using a Reynolds averaged Navier Stokes solver," Sci. Iran. **22**, 765–777 (2015).

Gray-Stephens, A., Tezdogan, T., and Day, S., "Numerical modelling of the near-field longitudinal wake profiles of a high-speed prismatic planing hull," J. Mar. Sci. Eng. **8**, 516 (2020).

Havelock, T. H., "The propagation of groups of waves in dispersive media, with application to waves on water produced by a travelling distance," Proc. R. Soc. London, Ser. A **81**, 398–430 (1908).

He, J., Wu, H., Yang, C., Li, W., and Noblesse, F., "Why can steep short waves occur at a ship waterline and how to filter them in a practical way?," Eur. J. Mech. -B/Fluids **83**, 164–174 (2020).

Hosseini, A., Tavakoli, S., Dashtimanesh, A., Sahoo, P. K., and Kõrgesaar, M., "Performance prediction of a hard-chine planing hull by employing different CFD models," J. Mar. Sci. Eng. **9**(5), 481 (2021).

ITTC, "Wave profile measurement and wave pattern resistance analysis," Report No. 7.5-02-02-04, 2021, Revision 00.

Jou, J., and Lo, W.-S., "Rogue waves associated with resonant slow sloshing waves spontaneously excited in wind-driven water wave turbulence," Phys. Fluids. **32**, 122120 (2020).

Judge, C., and Judge, J., "Measurements of hydrodynamic coefficients on a planing hull using forced roll oscillations," J. Ship Res. **57**(2), 112–124 (2013).

Keller, J. B., "Internal wave wakes of a body moving in a stratified fluid," Phys. Fluids **13**(6), 1425–1431 (1970).

Lamb, H., *Hydrodynamics* (Courier Corporation, 1932).

Lyden, J. D., Hammond, R. E., Lyzenga, D. R., and Shuchman, R. A., "Synthetic aperture radar imaging of surface ship waves," J. Geophys. Res. **93**, 12293–12303, https://doi.org/10.1029/JC093iC10p12293 (1988).

Ma, Y., Dong, G., Perlin, M., Ma, X., and Wang, G., "Experimental investigation on the evolution of the modulation instability with dissipation," J. Fluid Mech. **711**, 101–121 (2012).

Maki, K. J., Doctors, L. J., Beck, R. F., and Troesch, A. W., "Transom-stern flow for high-speed craft," Aust. J. Mech. Eng. **3**(2), 191–199 (2006).

Maki, K. J., Troesch, A. W., and Beck, R., "Experiments of two-dimensional transom stern flow," J. Ship Res. **52**(04), 291–300 (2008).

McCauley, J. L., "Hydrodynamic lift on boats," arXiv:1808.03313, 8 August (2018).

Moisy, F., and Rabaud, M., "Mach-like capillary-gravity wakes," Phys. Rev. E **90**, 023009 (2014a).

Moisy, F., and Rabaud, M., "Scaling of far-field wake angle of nonaxisymmetric pressure disturbance," Phys. Rev. E **89**, 063004 (2014b).

Mousaviraad, S. M., Zhang, W., and Stern, F., "URANS studies of hydrodynamic performance and slamming loads on high-speed planing hulls in calm water and waves for deep and shallow conditions," Appl. Ocean Res. **51**, 222–240 (2015).

Naghdi, P. M., and Rubin, M. B., "On the transition to planing of a boat," J. Fluid Mech. **103**, 345–374 (1981).

Niazmand Bilandi, R., Dashtimanesh, A., and Tavakoli, S., "Hydrodynamic study of heeled double-stepped planing hulls using CFD and 2D + T method," Ocean Eng. **196**, 106813 (2020).

Niazmand Bilandi, R., Dashtimanesh, A., and Tavakoli, S., "Seakeeping of double-stepped planing hulls," Ocean Eng. **236**, 109475 (2021).

Nobless, F., He, J., Zhu, Y., Hong, L., Zhang, C., Zhu, R., and Yang, C., "Why can ship wakes appear narrower than Kelvins angle?," Eur. J. Mech. B/Fluids **46**, 164–171 (2014).

O'Dea, J., Jenkins, D., and Nagle, T., "Flow characteristic of a transom stern ship," Report No. DTNSRDC-81/057 (David W. Taylor Naval Ship Research and Development Center, 1981).

Parnell, K. E., and Kofoed-Hansen, H., "Wakes from large high-speed ferries in confined coastal waters: Management approaches with examples from New Zealand and Denmark," J. Coast Manage. **29**(3), 217–237 (2001).
Patel, V. C., and Sarda, O. P., "Mean-flow and turbulence measurements in the boundary layer and wake of a ship double model," Exp. Fluids **8**, 319–335 (1990).
Paul, M., Bouma, T., and Amos, C., "Wave attenuation by submerged vegetation: Combining the effect of organism traits and tidal current," Mar. Ecol. Prog. Ser. **444**, 31–41 (2012).
Payne, P. R., "The water rise in front of a model planing hull," Exp. Fluids **17**, 96–104 (1994).
Pedersen, G., "Three-dimensional wave patterns generated by moving disturbances at transcritical speeds," J. Fluid Mech. **196**, 39–63 (1988).
Peregrine, D. H., "A ship's waves and its wake," J. Fluid Mech. **49**(2), 353–360 (1971).
Pethiyagoda, R., McCue, S. W., and Moroney, T. J., "Spectrograms of ship wakes: identifying linear and nonlinear wave signals," J. Fluid Mech. **811**, 189 (2017).
Pethiyagoda, R., Moroney, T., Macfarlane, G. J., and McCue, S. W., "Spectrogram analysis of surface elevation signals due to accelerating ships," Phys. Rev. Fluids **6**, 104803 (2021).
Rabaud, M., and Moisy, F., "Ship wakes: Kelvin or Mach angle?," Phys. Rev. Lett. **110**, 214503 (2013).
Reed, A. M., and Milgram, J. H., "Ship wakes and their radar images," Annu. Rev. Fluid Mech. **34**, 469–502 (2002).
Savitsky, D., "Hydrodynamic design of planing hulls," Mar. Technol. **1**(04), 71–95 (1964).
Savitsky, D., "Planing craft," Nav. Eng. J. **97**(2), 113–141 (1985).
Savitsky, D., "Wake shapes behind planing hull forms," in *Proceedings of the International Conference on High-Performance Vehicle Conference* (The Chinese Society of Naval Architecture and Marine Engineering, Shanghai, 1988), p. VII, Vol. 1–15.
Savitsky, D., and Brown, P. W., "Procedures for hydrodynamic evaluation of planing hulls in smooth rough water," Mar. Technol. **13**(4), 381–400 (1976).
Savitsky, D., and Morabito, M., "Surface wave contours associated with the forebody wake of stepped planing hulls," Mar. Technol. **47**(1), 1–16 (2010).
Shomina, O., Kapustin, I., and Ermakov, S., "Damping of gravity–capillary waves on the surface of turbulent fluid," Exp. Fluids **61**, 184 (2020).
Sorensen, R. M., "Ship-generated waves," Adv. Hydrosci. **9**, 49–83 (1973).
Stumbo, S., Fox, K., Dvorak, F., and Elliot, L., "The prediction, measurement, and analysis of wake wash from marine vessels," Mar. Technol. **36**, 248–260 (1999).
Suneela, J., Krishnankutty, P., and Anantha Subramanian, V., "Numerical investigation on the hydrodynamic performance of high-speed planing hull with transom interceptor," Ships Offshore Struct. **15**, S134 (2020).
Tagliafierro, B., Mancini, S., Ropero-Giralda, P., Domínguez, J. M., Crespo, A. J. C., and Viccione, G., "Performance assessment of a planing hull using the smoothed particle hydrodynamics method," J. Mar. Sci. Eng. **9**, 244 (2021).
Tavakoli, S., Niazmand Bilandi, R., Mancini, S., De Luca, F., and Dashtimanesh, A., "Dynamic of a planing hull in regular waves: Comparison of experimental, numerical and mathematical methods," Ocean Eng. **217**, 107959 (2020).
Thomson, R. E., and Emery, W. J., *Data Analysis Methods in Physical Oceanography*, 3rd ed. (Elsevier Science, Amsterdam, The Netherlands, 1998).
Thomson, W., and Kelvin, L., "On ship waves," Proc. Inst. Mech. Eng. **38**(1), 409–434 (1887).
Torsvik, T., Soomere, T., Didenkulova, I., and Sheremet, A., "Identification of ship wake structures by a time–frequency method," J. Fluid Mech. **765**, 229–251 (2015).
Tuck, E. O., Scullen, D. C., and Lazauskas, L., "Wave patterns and minimum wave resistance for high-speed vessels," in Proceedings of the 24th Symposium on Naval Hydrodynamics, Fukuoka, Japan, 8–13 July (2002).
Ursell, F., "On Kelvin's ship-wave pattern," J. Fluid Mech. **8**, 418–431 (1960).
Van Dyck, R. L., "Final engineering report on wake shapes of planing forms associated with high-speed water-based aircraft," Report No. 768 (Stevens Institute of Technology, 1960).
Wang, H., and Chen, K., "An investigation on internal waves generated by towed models under a strong halocline," Phys. Fluids **29**, 065104 (2017).
Whittaker, T., and Elsässer, B., "Coping with the wash. The nature of wash waves produced by fast ferries," Ingema **11**, 40–44 (2002).
Wu, H., Wu, J., He, J., Yang, C., and Noblesse, F., "Wave profile along a ship hull, short farfield waves, and broad inner Kelvin wake sans divergent waves," Phys. Fluids **31**, 047102 (2019).
Wu, T. Y., "Generation of upstream advancing solitons by moving disturbances," J. Fluid Mech. **184**, 75–99 (1987).
Wyatt, D. C., and Hall, R. E., "Analysis of ship-generated surface waves using a method based upon the local Fourier transform," J. Geophys. Res. **93**(C11), 14133–14164, https://doi.org/10.1029/JC093iC11p14133 (1988).
Yih, C.-S., and Zhu, S., "Patterns of ship waves II. Gravity-capillary waves," Q. Appl. Math. **47**, 35–44 (1989).
Yuan, Z., Chen, M., Jia, L., Ji, C., and Incecik, A., "Wave-riding and wave-passing by ducklings in formation swimming," J. Fluid Mech. **928**, R2 (2021).
Zavadsky, A., Benetazzo, A., and Shemer, L., "On the two-dimensional structure of short gravity waves in a wind wave tank," Phys. Fluids **29**, 016601 (2017).
Zavadsky, A., and Shemer, L., "Investigation of statistical parameters of the evolving wind wave field using a laser slope gauge," Phys. Fluids **29**, 056602 (2017).